PNAS RESEARCH ARTICLE | PHARMACOLOGY
BIOPHYSICS AND COMPUTATIONAL BIOLOGY

Structural and thermodynamic framework for PIEZO1 modulation by small molecules

Wenjuan Jiang[a], Tharaka D. Wijerathne[b], Han Zhang[c,d,e,f], Yi-Chun Lin[a], Sunhwan Jo[g], Wonpil Im[c,d,e,f], Jerome J. Lacroix[b,1], and Yun L. Luo[a,1]

Edited by Olga Boudker, Weill Cornell Medicine, New York, NY; received June 28, 2023; accepted October 12, 2023

Mechanosensitive PIEZO channels constitute potential pharmacological targets for multiple clinical conditions, spurring the search for potent chemical PIEZO modulators. Among them is Yoda1, a widely used synthetic small molecule PIEZO1 activator discovered through cell-based high-throughput screening. Yoda1 is thought to bind to PIEZO1's mechanosensory arm domain, sandwiched between two transmembrane regions near the channel pore. However, how the binding of Yoda1 to this region promotes channel activation remains elusive. Here, we first demonstrate that cross-linking PIEZO1 repeats A and B with disulfide bridges reduces the effects of Yoda1 in a redox-dependent manner, suggesting that Yoda1 acts by perturbing the contact between these repeats. Using molecular dynamics–based absolute binding free energy simulations, we next show that Yoda1 preferentially occupies a deeper, amphipathic binding site with higher affinity in PIEZO1 open state. Using Yoda1's binding poses in open and closed states, relative binding free energy simulations were conducted in the membrane environment, recapitulating structure–activity relationships of known Yoda1 analogs. Through virtual screening of an 8 million-compound library using computed fragment maps of the Yoda1 binding site, we subsequently identified two chemical scaffolds with agonist activity toward PIEZO1. This study supports a pharmacological model in which Yoda1 activates PIEZO1 by wedging repeats A and B, providing a structural and thermodynamic framework for the rational design of PIEZO1 modulators. Beyond PIEZO channels, the three orthogonal computational approaches employed here represent a promising path toward drug discovery in highly heterogeneous membrane protein systems.

mechanosensitive channel | PIEZO1 | Yoda1 | agonist efficacy | alchemical free energy calculations

Significance

Yoda1 is a synthetic small molecule activator of an essential mechanosensitive ion channel called PIEZO1. While Yoda1 is currently the most widely used PIEZO channel modulator, its weak efficacy and pharmacokinetics preclude clinical use. Understanding how Yoda1 activates PIEZO1 would shed light on the gating operation of the channel and help design more potent modulators that could be beneficial for many clinical conditions. Here, we combine experiments and molecular dynamics simulations to show that Yoda1 acts like a molecular wedge by inserting itself between two transmembrane domains located near the channel pore and stabilizes PIEZO1 open state. Additionally, we report two PIEZO1 activators identified through virtual screening. This study hence paves the way for the rational design of PIEZO1 modulators.

The ability of cells to rapidly transduce mechanical deformations of their membrane into intracellular electrochemical signals is essential to many important physiological functions, ranging from the senses of touch and body position to homeostatic processes underlying cell volume and blood pressure regulation. In vertebrates, this task is mainly achieved by mechanosensitive PIEZO1 and PIEZO2 ion channels (1). PIEZOs possess a unique homotrimeric structure that consists of a central pore region and three large flexible arms that curve or flatten as a function of the local membrane curvature (2–12).

Genetic PIEZO1 variants associated with gain or loss of function are associated with numerous conditions, suggesting the possibility that pharmacological PIEZO1 modulators could yield clinical benefits. In the cardiovascular system, for instance, PIEZO1 activators could mimic beneficial effects of exercise (13) and prevent malaria-causing *Plasmodium* infection of red blood cells (14, 15). PIEZO1 activators could also help treat lymphedema, a common side effect of breast cancer surgery (16, 17), promote muscle regeneration (18), and bone formation (19). On the other hand, PIEZO1 inhibitors are predicted to reduce cartilage injury and posttraumatic osteoarthritis (20), prevent pancreatitis (21), reduce mechanical itch (22), and help fight certain forms of cancer (23–25). Beyond the clinic, PIEZO1 modulators would also help further delineate the biological roles of PIEZO1 and help understand how discrete protein motions of channel domains control opening and closure of the pore.

In this context, a PIEZO1-selective small-molecule activator named Yoda1 was discovered through high-throughput screening of 3.25 million compounds using a cell-based fluorescence assay (26). Yoda1 increases PIEZO1 open probability, as evidenced by modulation of several biophysical parameters, including a reduction of the mechanical threshold for activation, a slowing down of macroscopic inactivation and deactivation kinetics, and a reciprocal modulation of microscopic open and shut dwell times (26, 27). Yoda1 physically interacts with PIEZO1's arm domain (9), and its effects are abolished when gating motions of the arms and/or the cap are inhibited with disulfide bridges (27).

The arms of PIEZO channels consist of a juxtaposition of nine transmembrane bundles known as PIEZO repeats A to I, each repeat encompassing four transmembrane helices.

Author contributions: W.I., J.J.L., and Y.L.L. designed research; W.J., T.D.W., H.Z., Y.-C.L., S.J., J.J.L., and Y.L.L. performed research; W.I., J.J.L., and Y.L.L. contributed new reagents/analytic tools; W.J., T.D.W., H.Z., Y.-C.L., S.J., J.J.L., and Y.L.L. analyzed data; and W.J., T.D.W., H.Z., S.J., J.J.L., and Y.L.L. wrote the paper.

Competing interest statement: S.J. was employed by SilcsBio at the time of manuscript preparation.

This article is a PNAS Direct Submission.

[1]To whom correspondence may be addressed. Email: jlacroix@westernu.edu or luoy@westernu.edu.

This article contains supporting information online at https://www.pnas.org/lookup/suppl/doi:10.1073/pnas.2310933120/-/DCSupplemental.

Published December 7, 2023.

We previously discovered that PIEZO1 repeat A harbors a minimal region (residues 1961 to 2063 in mouse PIEZO1) essential for Yoda1's effects (28). Using all-atom molecular dynamics (MD) simulations, we observed that Yoda1 spontaneously partitions into the membrane and diffuses into a hydrophobic pocket sandwiched between repeats A and B (Fig. 1*A*), whereas steric (alanine to tryptophane) mutations in this pocket abrogate or reduce Yoda1-mediated PIEZO1 activation (29).

In this study, we provide experimental and quantitative computational evidence supporting a pharmacological model in which Yoda1 acts as a wedge between repeats A and B and stabilizes PIEZO1 open conformation. We first show that cross-linking repeats A and B with disulfide bridges reduces the effects of Yoda1 in a redox-dependent manner. We next took advantage of our previous computational PIEZO1 open state model (7) to compare Yoda1's binding affinity between closed and open channel conformations. MD-based absolute binding free energy (ABFE) calculations show that Yoda1 adopts a deeper binding pose in the open state, enabling the molecule to bind the open state stronger, consistent with the thermodynamic property of any ligand acting as allosteric activator. Next, we used relative binding free energy (RBFE) calculations to understand structure–activity relationship (SAR) for seven Yoda1 analogs and identify correlations between Yoda1's chemical structure and changes in binding affinity and/or agonist efficacy. We finally exploit Yoda1's binding site using the site identification by ligand competitive saturation (SILCS) method (30, 31) in the membrane environment to virtually screen 8 million compounds, leading us to identify two PIEZO1 activators with

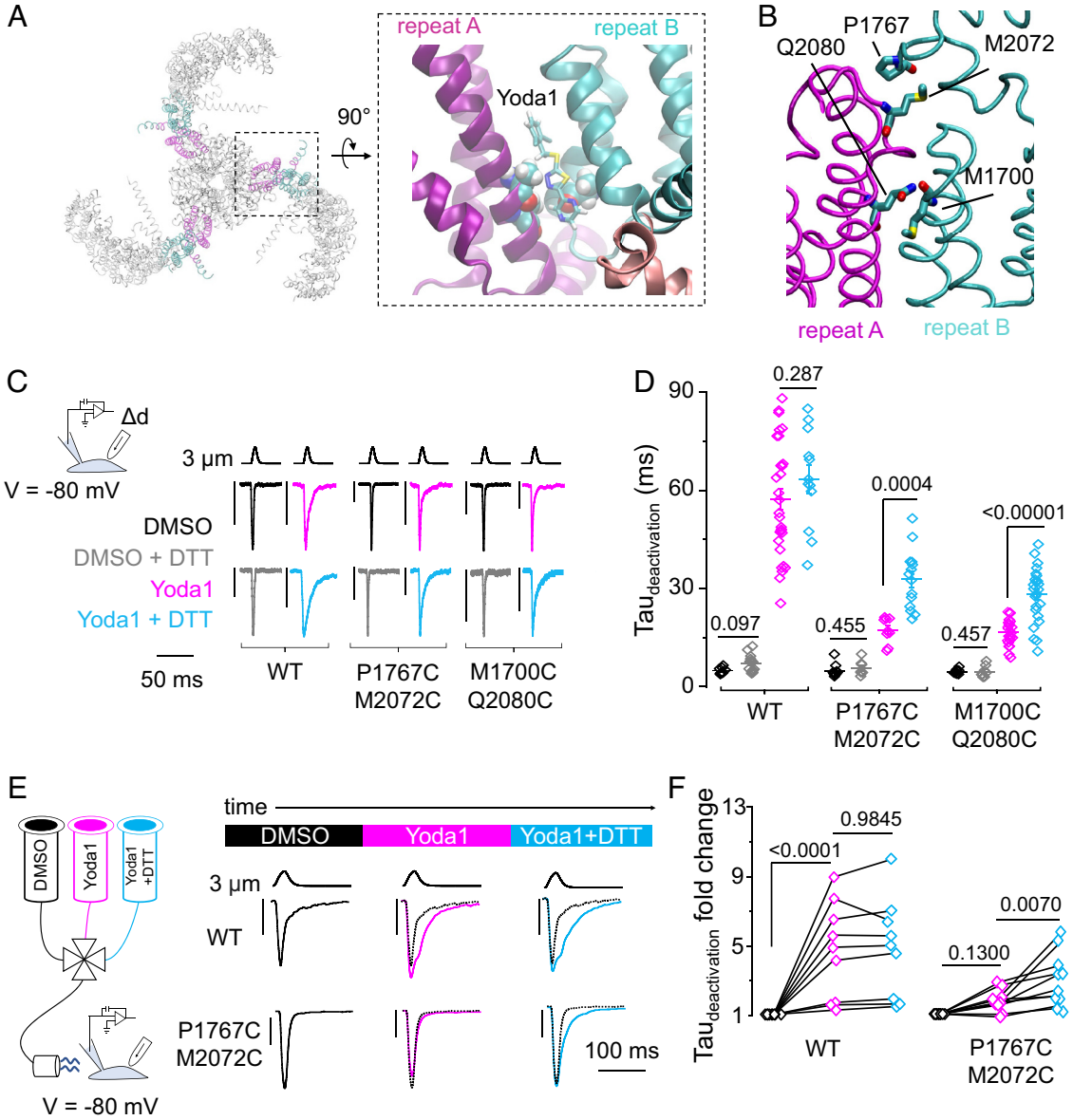

Fig. 1. Cross-linking repeat A with repeat B reduces the effects of Yoda1. (*A*) *Left*: Top view of PIEZO1 (PDB ID:6b3r) showing its repeat arrangement along the arm (colored letters). *Right*: Yoad1 binding pose (indicated by the arrow) sandwiched between repeats A and B. The illustration is adapted from ref. 29. (*B*) Location of candidate residues for cysteine mutagenesis shown on the AlphFold2 mPIEZO1 structural model. (*C*) Representative poke recordings obtained in indicated static incubations (0.075% DMSO, 0.075% DMSO + 10 mM DTT, 30 μM Yoda1, 30 μM Yoda1 + 10 mM DTT) from cells expressing WT mPIEZO1 or the indicated mutant (vertical bars = 200 pA). (*D*) Scatter plots of $Tau_{deactivation}$ recorded from experiments shown in (*C*). Each diamond represents an independent cell. Numbers above plots are exact *P* values from a Student's *t* test. (*E*) Representative poke recordings obtained in cells expressing WT mPIEZO1 or the indicated mutant and sequentially perfused with 0.075% DMSO, 30 μM Yoda1, and 30 μM Yoda1 + 10 mM DTT bath solutions (vertical bars = 200 pA). (*F*) Scatter plots showing changes of $Tau_{deactivation}$ relative to DMSO for WT mPIEZO1 and the P1767C/M2072C mutant. Number above plots indicate exact *p* value from repeated measures ANOVA with Tukey's multiple comparison tests.

distinct scaffolds. All three MD-based methods employed in this study (i.e., ABFE, RBFE, SILCS) were conducted in an explicit membrane environment, thus representing promising approaches for drug discovery at the protein-membrane interface.

Results

Cross-Linking PIEZO1 Repeat A with Repeat B Diminishes the Effects of Yoda1. The location of our putative binding site suggests that Yoda1 acts like a wedge, separating the extracellular side of repeats A and B from each other (29). According to this model, inhibiting this motion should also abolish the agonist effects of Yoda1. A simple way to test this prediction is to cross-link extracellular sites of repeats A and B using engineered cysteine bridges. Indeed, exposure of cysteine to the oxidative bulk solution should promote the spontaneous formation of a disulfide bridge, providing the two cysteine side chains are closed to each other (i.e., Cα-Cα distance < ~8 Å). Accessibility to the bath solution also conveniently enables reduction of cysteine bridges with a cysteine-reducing agent such as dithiothreitol (DTT), a necessary step to correlate functional phenotypes with the presence of disulfide bridge(s). Based on these criteria, we examined a partial high-resolution cryo-EM mPIEZO1 structure (PDB ID:6b3r) (5) as well as the full-length PIEZO1 structural model predicted by AlphaFold2 (32) to seek possible candidate residues located in extracellularly accessible positions in repeats A and B. This led us to identify two pairs of candidate residues: P1767/M2072 (Cα-Cα distance = 5.44 Å in the AlphaFold2 model) and M1700/Q2080 (Cα-Cα distance = 6.30 Å in the AlphaFold2 model and 5.88 Å in the 6b3r structure) (Fig. 1*B*).

We measured the effects of Yoda1 in these mutants using whole cell poking electrophysiology. To this aim, we transiently expressed wild-type (WT) mouse PIEZO1 (mPIEZO1) or one of the double cysteine mutants into PIEZO1-deficient HEK293T$^{\Delta PZ1}$ cells (33). On the day of experiments, these cells were immersed in a bath solution supplemented with Yoda1 or dimethyl sulfoxide (DMSO) vehicle control and supplemented or not with DTT. A recording pipette was then quickly sealed against the cell membrane and suction was subsequently applied to electrically access the interior of the cell. Whole-cell PIEZO1 currents were measured using brief (40 ms) indentations with a glass probe. We focused on macroscopic deactivation kinetics since this gating parameter was shown to be the most sensitive to the presence of Yoda1 (27). Fitting the time course of deactivation currents ($Tau_{deactivation}$) with a mono-exponential function reveals that WT PIEZO1 deactivates ~12-fold slower in the presence vs. absence of Yoda1 (~60 ms vs. ~5 ms), while DTT does not significantly affect deactivation kinetics ($0.097 < P$ values < 0.287) (Fig. 1 *C* and *D*). In the mutants, however, the presence of DTT correlates with a ~twofold slowing down of deactivation kinetics in the presence (~30 ms vs. ~15 ms; $0.00001 < P$ values < 0.0004) but not in the absence (~5 ms; $0.455 < P$ values < 0.457) of Yoda1.

Compared to WT PIEZO1, these mutants exhibit a smaller response to Yoda1 in the presence of DTT. This difference could be due to a decrease of Yoda1's affinity and/or efficacy caused by the presence of the two cysteine substitutions near Yoda1's binding site. These mutants also seem to display basal sensitivity to Yoda1 in the absence of DTT. This residual sensitivity could be due to a noncomplete oxidation of the thiol groups, meaning that the cysteines pairs may not form a disulfide bridge in all PIEZO arms. It could also be due to the fact that a single disulfide bridge, cross-linking one of repeat A's α-helix to one of repeat B's α-helix, may not be sufficient to completely eliminate the effects of Yoda1, as each repeat encompasses four α-helices. Nevertheless, the fact that DTT significantly slows down deactivation kinetics in the presence of Yoda1 in both mutated, but not WT, channels shows that these cross-links specifically reduce the effects of Yoda1.

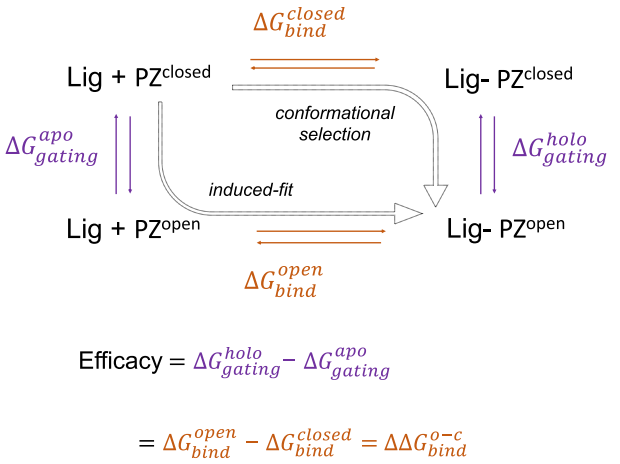

Fig. 2. Thermodynamics of ion channel modulation by an allosteric ligand. The figure shows a thermodynamic cycle linking the efficacy of a ligand (Lig) to its binding affinities toward a PIEZO channel (PZ) in an open or closed state. ΔG_{gating}^{apo} and ΔG_{gating}^{apo} refer to the free energy difference between open and closed states in the presence (holo) or absence (apo) of the bound ligand.

We next used a continuous perfusion system to sequentially apply bath solutions containing DMSO, Yoda1 and Yoda1+DTT while cells are continuously electrophysiologically tested using poke stimuli. We focused on the P1767C/M2072C mutant because its DTT response in the presence of Yoda1 appears larger compared to the M1700C/Q2080C mutant. Brief poke stimuli were delivered every 20 s to continuously monitor deactivation kinetics. Deactivation currents significantly slowed down in WT channels shortly after switching the external solution from DMSO to Yoda1 and remained slow after subsequent DTT addition (Fig. 1 *E* and *F*). By contrast, deactivation currents in the mutant did not significantly slowdown in the presence of Yoda1 alone (repeated measures ANVOA with Tukey's multiple comparisons *P* value = 0.130) but did so after DTT addition (*P* value = 0.007), consistent with results obtained from nonpaired experiments. Taken together, these electrophysiology data support the hypothesis that Yoda1 mediates its effects by wedging repeats A and B.

Thermodynamics Framework of Allosteric Activators. Allosteric ion channel activators are predicted to energetically promote a ligand-bound open state, either through conformational selection (selective binding to the open state) or through induced fit (ligand-induced gating motions) (Fig. 2). Regardless of the pharmacological pathway taken, the thermodynamic law of energy conservation states that the extent of channel activation produced upon ligand binding (efficacy) is energetically equivalent to the difference of binding affinity between open (o) and closed (c) states, i.e., $\Delta G_{bind}^{open} - \Delta G_{bind}^{closed} = \Delta\Delta G_{bind}^{o-c}$.

Following this thermodynamic principle, allosteric ion channel activators exhibit a stronger binding affinity for the open state ($\Delta\Delta G_{bind}^{o-c} < 0$), allosteric inhibitors exhibit a stronger affinity for the closed state ($\Delta\Delta G_{bind}^{o-c} > 0$), and nonactive binders (i.e., silent binders) are predicted to bind both states indistinguishably ($\Delta\Delta G_{bind}^{o-c} \approx 0$).

Inspecting Yoda1 Binding Poses from Unbiased MD Simulations. Conducting binding free energy simulation with the entire PIEZO1 trimer (~7,500 aa) is computationally expensive and inefficient. Since

state-dependent binding affinity is primarily determined by the local binding environment (e.g., the composition and dynamics of protein, lipids, water within 20 Å of ligand), we simulated a truncated single PIEZO1 arm (residue 1131 to 2190) embedded in a lipid bilayer in closed (29) and open (7) states (*Materials and Methods*).

Starting from previously identified Yoda1 binding pose in the closed state, five replicas of 100 ns unbiased MD simulations were carried out for Yoda1-closed and Yoda1-open single arm systems. We found that the Yoda1 binding pose in the closed state is consistent with our previous 4.8 μs simulation in PIEZO1 trimer (29), and the ligand-lipid contact is negligible (Fig. 3*A*). In the open state, Yoda1 occupies a deeper pocket between repeat A and B toward the intracellular side. In this amphipathic binding pocket in open state, Yoda1's dichlorophenyl moiety makes stable hydrophobic contacts with protein (F1715, V1714, and I1696) and lower leaflet lipid tails, while the pyrazine moiety of Yoda1 is highly mobile, forming dynamic contacts with the protein, lipid headgroups, and water molecules (Fig. 3*B* and see *SI Appendix*, Fig. S9 for water and lipid atoms inside the pocket).

These observations from unbiased MD trajectories suggest that the dichlorophenyl group acts as an anchor to secure Yoda1 in the hydrophobic binding site, and that chemical modifications of the mobile pyrazine group might be tolerated. This opens the door to rationally optimize the Yoda1 scaffold through chemical extensions, for instance through addition of hydrophilic chemical groups promoting interactions with the intracellular side of the binding pocket.

Absolute binding free energy (ABFE) of Yoda1. Yoda1's state-dependent binding affinity would be difficult to validate experimentally. But it can be probed computationally. Indeed, since free energy is a state function, ABFE can be computed alchemically using free energy perturbation (FEP). This is generally done by scaling a thermodynamic coupling parameter, λ, from 1 to 0, allowing us to gradually turn off nonbonded interactions between the ligand and its environment in both bound and unbound states (i.e., double-decoupling scheme) (34). The free energy difference between the bound and unbound states (i.e., ABFE or ΔG_{bind}) is related to the dissociation constant by $K_d = C^o e^{\beta \Delta G_{bind}}$. We assume that at thermodynamic equilibrium, membrane partitioning of the ligand is an intermediate state which does not need to be computed explicitly (see Table 1 diagram). Thus, the ABFE computed here corresponds to the free energy difference between a ligand in the bulk solution at standard concentration (C^o = 1 mol/L) and the same ligand in the binding site.

Starting from the most populated Yoda1 binding poses extracted from unbiased simulations (Fig. 3), we computed ABFEs using FEP coupled with replica-exchange MD (FEP/REMD) implemented in NAMD (35) using the CHARMM36 force field for the protein (36) and CGenFF force field (37, 38) for ligand. To taking into account the flexibility of the ligand at the protein–membrane interface and to facilitate FEP/REMD convergence, a set of flat-bottom harmonic restraints between protein and ligand were customized based on the conformational ensemble from the 500 ns unbiased simulations above. These restraints essentially allow unbiased sampling of the fully coupled ligand (λ = 1 stage) and prevent the decoupled ligand (λ = 0 stage) to wander outside the binding site (*Materials and Methods* and *SI Appendix*, Fig. S1).

To check whether our FEP/REMD simulations correctly sample the end states during the massive replica exchange over 128 λ values, we compared the number of water and lipid atoms inside the binding pocket between unbiased sampling and the fully coupled (λ = 1) stage (*SI Appendix*, Fig. S9). In both cases, there are ~20 lipid atoms occupying the open pocket, while lipids are nearly absent in the closed pocket. When the ligand is fully uncoupled (λ = 0), more lipid atoms occupied the open pocket.

Yoda1's binding affinity (K_d) of 45.6 ± 14.3 μM, experimentally measured against detergent-purified mPIEZO1 (9), corresponds to a binding free energy of approximately –6.0 kcal/mol at room temperature. This value is close to our computed –6.8 ± 0.2 kcal/mol for Yoda1 against the closed state, i.e., the conformation thought to be predominantly populated in detergent micelles. Notably, our ABFE results indicate that Yoda1 binds the open state stronger than the closed state ($\Delta\Delta G^{o-c}_{bind}$ = –3.7 ± 0.3 kcal/mol), consistent with its agonist effect (Table 1 and *SI Appendix*, Table S1).

As a negative control, we also computed ABFEs for Dooku1, a nonactive analog that antagonizes Yoda1's agonist effect (39). Our results show that Dooku1 binds to the closed state slightly stronger than Yoda1 but binds the open state weaker than Yoda1, consistent with Dooku1's ability to inhibit the effects of Yoda1 while lacking detectable agonist activity toward PIEZO1 (27, 39). We also noticed from our unbiased simulations that, while the poses taken by Yoda1 and Dooku1 are similar in the closed state, Yoda1 binds lower within the open state pocket compared to Dooku1 (*SI Appendix*, Fig. S1). To investigate whether this could be attributed to sampling artifacts, we manually switched Yoda1 and Dooku1 binding positions in the open state and conducted two additional ABFE simulations. These calculations confirmed that Yoda1 preferentially populates the lower binding pocket and that Dooku1 binds to both positions indiscriminately (*SI Appendix*, Table S1). In conclusion, based on our two-state model (Fig. 2), the ABFE results show that Yoda1, but not Dooku1, preferentially binds the open state, thus stabilizes the open conformation of PIEZO1 channel.

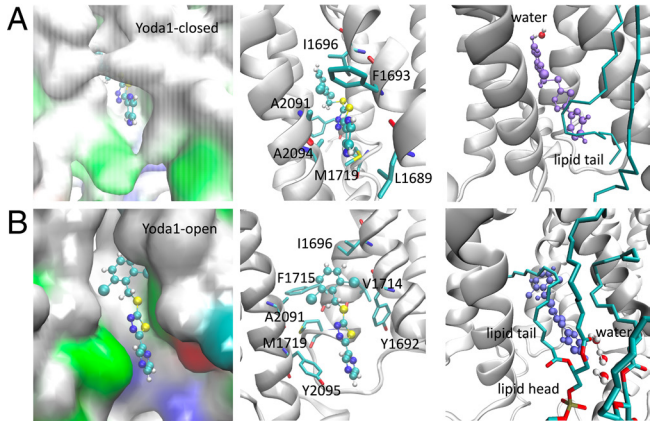

Fig. 3. Yoda1 binding poses in PIEZO1 closed (*A*) and open (*B*) states. (*Right*): Yoda1 in CPK mode and protein in surface mode. (*Middle*): protein in new cartoon mode with residues within 3 Å of Yoda1 shown in licorice mode, (*Left*): Lipid and water molecules within 3 Å of Yoda1 are shown in licorice mode. Atom color: cyan carbon or chloride, blue nitrogen, red oxygen, and yellow sulfur.

Relative binding free energy (RBFE) of Yoda1 Analogs. ABFE is computationally expensive because the alchemical perturbation must be done for the whole ligand. RBFE calculations, on the other hand, are more efficient to study a set of analogs that only differ by small chemical modification. We hence use RBFE to cross-validate our ABFE results for Yoda1 and Dooku1, and to predict efficacy of other Yoda1 analogs.

Using Yoda1 as the reference compound, we define RBFE as $\Delta\Delta G = \Delta G^{analog}_{bind} - \Delta G^{Yoda1}_{bind}$ (see Table 2 diagram). Thus, Yoda1 analogs having $\Delta\Delta G < 0$ for a given conformation are predicted to bind this conformation stronger than Yoda1, and vice versa. In addition, following thermodynamic principles in Fig. 2, we define

Table 1. ABFE for Yoda1 and Dooku1 in PIEZO1 open and closed state

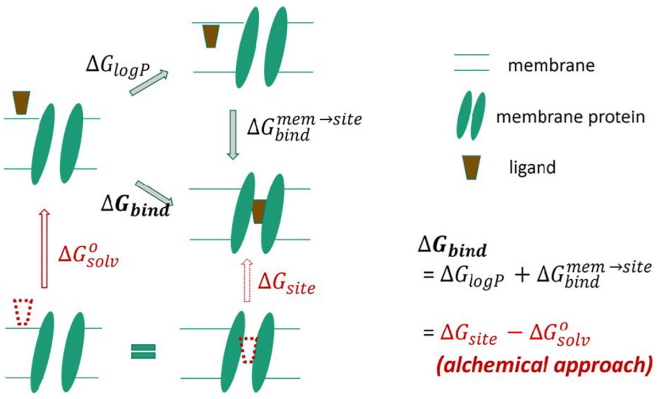

Free energy (kcal mol^{-1})	Yoda1 closed state	Yoda1 open state	Dooku1 closed state	Dooku1 open state
ΔG_{bind}	−6.8 ± 0.2	−10.5 ± 0.2	−9.7 ± 0.6	−8.1 ± 0.2
ΔG_{bind}^{o-c}	−3.7 ± 0.3		1.6 ± 0.6	

The thermodynamic cycle used to compute ΔG_{bind} illustrated in red. The individual free energy components and the uncertainty estimation are summarized in *SI Appendix*, Table S1.

$\Delta\Delta G^{open} - \Delta\Delta G^{closed} = \Delta\Delta\Delta G^{o-c}$ as the efficacy of an analog relative to Yoda1. Hence, ligands having $\Delta\Delta\Delta G^{o-c} < 0$ are predicted to act as better agonists than Yoda1. In theory, ligands having positive $\Delta\Delta\Delta G^{o-c}$ larger than Dooku1 could potentially act as PIEZO1 inhibitors by promoting a closed conformation.

RBFE was carried out using the same system as in ABFE, including water and membrane. A total of 14 × 4 replicas of RBFE simulations were carried out to compute the free energy cost of converting Yoda1 to Dooku1 and six other analogs (39, 40) in the PIEZO1 open and closed states. All RBFE simulations were conducted using GPU accelerated AMBER-TI method (41, 42) with AMBER ff19SB force field (43) for protein and GAFF2.1 (44) for ligands. Similar to ABFE results, RBFE calculations indicate that Dooku1 binds the PIEZO1 open state weaker than Yoda1 ($\Delta\Delta G^{open}$ = 1.19 ± 0.49 kcal/mol) but binds the closed state stronger than Yoda1 ($\Delta\Delta G^{closed}$ = −1.90 ± 0.62 kcal/mol) (Table 2). The concurrence between ABFE and RBFE results, obtained using two distinct methods and force fields, provided a good validation of the computational models and approaches employed here.

RBFE results in Table 2 revealed key SAR and explained gain/loss in agonist activity in terms of the changes in binding affinity or agonist efficacy. For instance, removing ring A's two chlorine atoms reduces binding affinity in both states (**1a**), whereas adding a fluorine to this ring slightly increases binding to the open state (**2a**). In addition, replacing Yoda1's ring D by pyrrole (Dooku1 and **7b**) weakens binding to the open state but strengthens binding to the closed state, leading to efficacy loss. Replacing ring D by phenyl (**2i**) increases binding to both states but reduces efficacy, whereas replacing a sulfur atom by oxygen in ring C (**11**) or by sulfone in linker B (**1b**) reduces affinity to both states. The affinity loss seen in **11** and **1b** is likely due to the fact that these sulfur replacements prevent ring A to adopt a stable binding pose, as ring A becomes highly mobile during the simulation. Overall, RBFE calculations provided a thermodynamic rationale underlying the SAR of agonist activities reported from cell-based functional assays (39, 40).

Beyond the reported Yoda1 analogs, RBFE can be used to evaluate more drug-like linker B structures. It can also be used to extend the ring D structure to take advantage of the larger and more hydrophilic open pocket. As more Yoda1 analogs are synthesized and tested, the state-dependent RBFE results can serve as a powerful tool for fine-tune the design by biasing the binding toward open state for more potent agonists or toward the closed state for potential inhibitors.

Rapid Ranking of Yoda1 Analogs Using Fragment Maps. Yoda1 was discovered by screening ~3.25 million small molecules (26). This seemingly large number represents only a tiny fraction of the estimated small molecule chemical space [e.g., 10^{60} for molecules harboring 30 heavy atoms (45)]. Knowledge of the Yoda1 binding site provides an opportunity to expand PIEZO1 modulators beyond Yoda1 scaffold.

Site Identification by Ligand Competitive Saturation (SILCS) (30, 31) has recently shown promising ranking power for ligands bound to membrane proteins (46). In SILCS method MD simulations of PIEZO1 are conducted in solvated bilayer, along with drug fragments (benzene, propane, methanol, aryl halide, imidazole, etc.) in water. During simulations, Grand Canonical Monte Carlo/MD (GCMC/MD) method that oscillates chemical potential is used to accelerate protein-fragment binding/unbinding events (47), enabling the creation of three-dimensional fragment density maps (FragMaps) of target proteins in a realistic membrane environment. Furthermore, in SILCS version 2020.1, halogen atoms are treated with lone pairs to achieve directionality in polar interactions, which makes SILCS an appealing approach for testing the Yoda1 analogs.

Using the same simulation system as in ABFE and RBFE, we generated FragMaps of the PIEZO1 arm using 10 replicas of 100 ns SILCS GCMC/MD simulations (Fig. 4*A*). Ligand docking to FragMaps was performed using the SILCS-Monte Carlo (SILCS-MC) sampling method. Five independent SILCS-MC samplings were conducted, and the results were considered converged when the deviation of the lowest ligand gride free energy (LGFE) was less than 0.5 kcal/mol. Using SILCS-MC global docking, we found that the lowest LGFE pose of Yoda1 not only matches the Yoda1 pose obtained from ABFE simulations but also explains SAR data. For instance, Yoda1's dichlorophenyl matches FragMap densities of chlorobenzene and fluorobenzene (Fig. 4*A*). It is thus not surprising that removing chlorine substituents reduces binding affinity, whereas replacing them by the fluorine group increases affinity (26, 39, 40), which was also shown in RBFE results above.

SILCS predicts that Yoda1 binds slightly stronger than Dooku1 in the open state, following the same trend seen in ABFE and RBFE (Fig. 4*B*). Interestingly, while all three computational methods qualitatively agree, their sensitivity (in differentiating Yoda1 vs. Dooku1) decreases as the computational cost decreases. In contrast, the popular virtual screening tool AutoDock Vina (48) was unable to discriminate Yoda1 and Dooku1 in this study, possibly due to the missing membrane environment in Vina scoring function.

Virtual Screening and Identification of PIEZO1 Activators. Overall, a Pearson correlation coefficient of 0.68 between RBFE (Table 2) and SILCS results for Yoda1 analogs in open state suggests that SILCS is suitable for virtual screening of PIEZO1 binders (Fig. 4*C*, see docking poses in *SI Appendix*, Fig. S12). SILCS-PHARM software (SilcsBio, LLC) (49) was used to convert the SILCS FragMaps at the Yoda1 binding region into pharmacophore features. These pharmacophore features were used to search 8 million commercially available compounds (provided by MolPort) using the program Pharmer (50) (Fig. 4*A*) (*Materials and Methods*). We purchased top 155 compounds and individually tested their activatory effects at 150 μM using calcium imaging.

Table 2. Relative binding free energy (RBFE) results for Yoda1 and its analogs

$$\Delta\Delta G^{open} = \Delta G^{open}_{site} - \Delta G_{bulk} \qquad \Delta\Delta G^{closed} = \Delta G^{closed}_{site} - \Delta G_{bulk}$$

$$\Delta\Delta\Delta G^{o-c} = \Delta\Delta G^{open} - \Delta\Delta G^{closed} = \Delta G^{open}_{site} - \Delta G^{closed}_{site}$$

Name	Structure	$\Delta\Delta G^{open}$	$\Delta\Delta G^{closed}$	$\Delta\Delta\Delta G^{o-c}$	RBFE prediction	Agonist activity (39, 40)
Yoda1	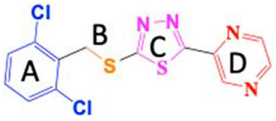	0	0	0	Reference	100%
Dooku1	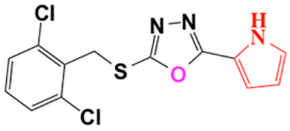	1.19 ± 0.49	−1.90 ± 0.62	3.09 ± 0.79	Efficacy loss	No
7b	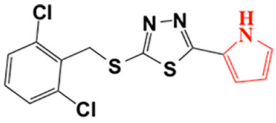	1.13 ± 0.28	−0.59 ± 0.41	1.72 ± 0.50	Efficacy loss	<50%
2i	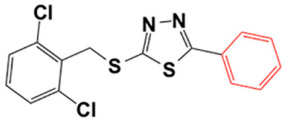	−1.24 ± 0.42	−2.58 ± 0.16	1.34 ± 0.45	Efficacy loss	<50%
11	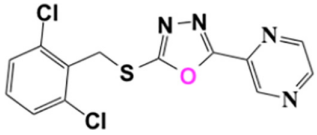	1.63 ± 0.18	1.87 ± 0.24	−0.24 ± 0.30	Affinity loss	70%
1b	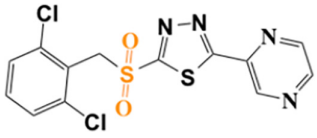	3.47 ± 0.26	3.18 ± 0.31	0.29 ± 0.40	Affinity loss	No
1a	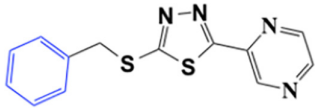	1.9 ± 0.26	2.49 ± 0.35	−0.59 ± 0.44	Affinity loss	No
2a	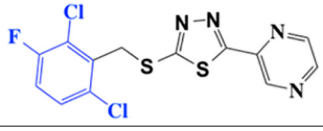	−0.42 ± 0.07	−0.08 ± 0.15	−0.34 ± 0.17	Efficacy gain	>100%

SDs are computed from four replicas of 5 to 10 ns AMBER-TI runs (see *SI Appendix*, Fig. S10*B*). Qualitative experimental agonist activities are from refs. 39 and 40. The RBFE thermodynamic cycle is illustrated above.

Among them, two compounds elicit calcium uptake above DMSO control, namely CMPD15 and CMPD64 (Fig. 5 *A* and *B* and *SI Appendix*, Fig. S12). The dose–response curve of CMPD15, obtained by plotting maximal $\Delta F/F_0$ values against ligand concentration, was fitted to a standard binding function and the results were compared to those obtained with Yoda1 (Fig. 5*C*). CMPD15 exhibits a lower maximal efficacy (Emax) than Yoda1 (0.21 ± 0.04 vs. 0.97 ± 0.21 $\Delta F/F_0$) but its EC50 (12.9 ± 4.73 μM) is similar to that of Yoda1 (18.4 ± 8.8 μM). In contrast to CMPD15, CMPD64 produces only a small increase of calcium-dependent fluorescence at 150 μM (Fig. 5*D*), precluding accurate estimation of EC50 and Emax from dose–response measurements.

In whole-cell poking experiments, supplementing the bath solution with CMPD15 or CMPD64 correlates with a slowing down of both deactivation and inactivation kinetics compared to DMSO vehicle control (Fig. 5 *E* and *F*), an effect that was statistically significant at the standard 5% threshold for CMPD15 (*P*

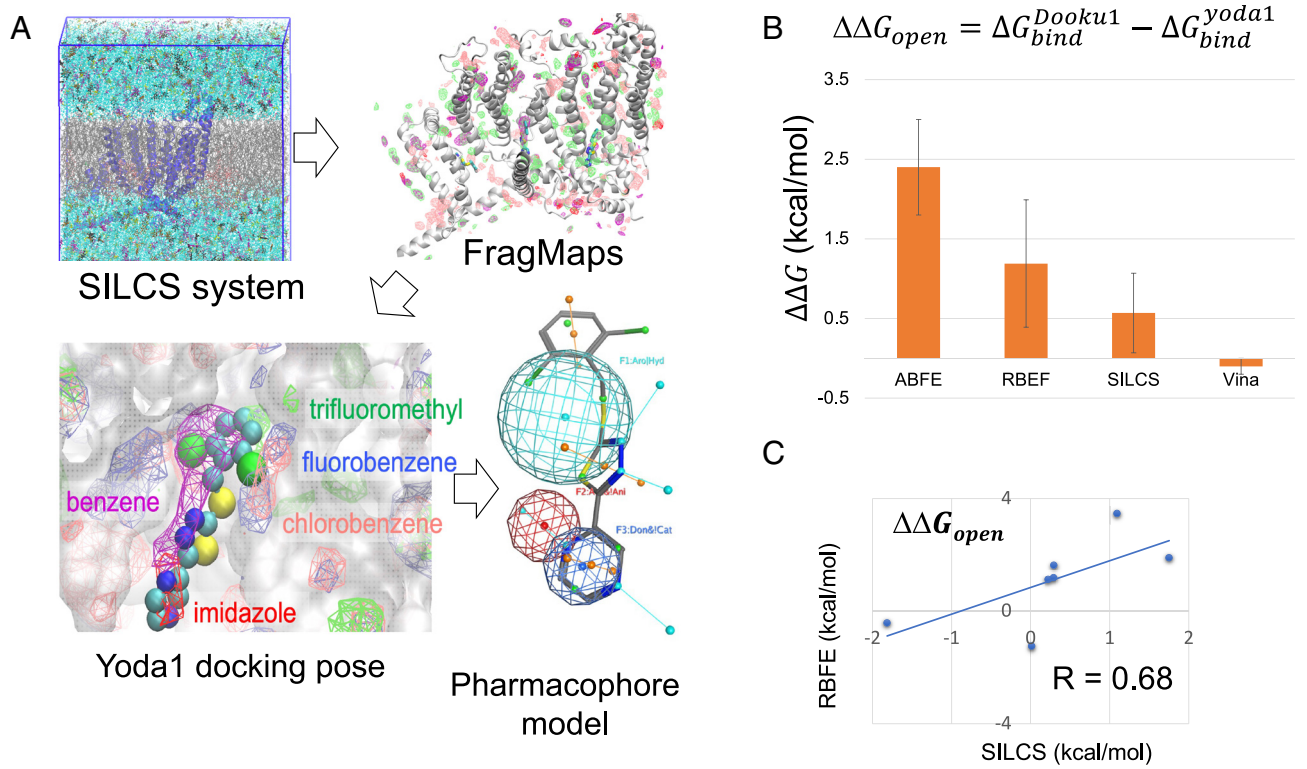

Fig. 4. FragMaps of Yoda1 binding site and ranking power of SILCS. (*A*) SILCS simulations of PIEZO1 arm in open state, PIEOZ1 FragMaps, the top binding pose of Yoda1 overlaid with FragMaps, and overlaid with SILCS pharmacophore model generated from FragMaps. (*B*) Binding free energy difference between Yoda1 and Dooku1 in PIEZO1 open state, from ABFE, RBFE, SILCS, and AutoDock Vina. (*C*) Pearson correlation coefficient between RBFE and SILCS results for Yoda1 analogs (Table 2) in open state.

values ≤ 0.0068) but not for CMPD64 (0.0804 < *P* values < 0.1096). This difference mirrors our calcium imaging results showing a weaker modulatory effect by CMPD64. As negative controls, we electrophysiologically tested five other compounds. Neither of them modulate PIEZO1 inactivation (*P* values ≥ 0.9997) or deactivation (*P* values ≥ 0.4070) kinetics (Fig. 5*F*). Overall, our screening results identify two bona fide PIEZO1 activators with distinct scaffolds, thus validating the interface between repeats A and B as an exploitable pharmacological region.

Discussion

Drugs that positively or negatively modulate PIEZO1 channel are highly sought after. Years of synthetic efforts to derivatize Yoda1 have yielded only modest pharmacological improvements (40, 51). The challenges in optimizing Yoda1 may stem from both the lack of information on the binding site and Yoda1's linear and rigid scaffold. Our previous MD simulations and mutagensis studies identified a putative Yoda1 binding site at PIEZO1's transmembrane regions between repeats A and B. However, direct structural evidence of this binding site is still lacking. Due to the large size of PIEZO1 (~7,500 amino acids) and the low solubility of Yoda1, solving the structure of a Yoda1-PIEZO1 complex at high resolution remains challenging. Moreover, silent binding sites (i.e., with no agonist effect) may exist due to the sheer size of PIEZO1 (~1.2 million Daltons) and the hydrophobic nature of Yoda1 (355 Daltons, cLogP 3.5).

Our recently generated in silico PIEZO1 open state model with flattened arms (7) offered an opportunity to interrogate the thermodynamic framework of Yoda1 at this binding region more quantitively. Although PIEZO1 is thought to populate multiple open and closed microscopic states (26, 27, 52, 53), the availability of both closed and open PIEZO1 structural models provides a simple two-state thermodynamic framework to validate Yoda1's agonist activity by computing the binding free energy differences between the open and closed states ($\Delta\Delta G_{bind}^{o-c}$). This strategy obviates the need to deploy computationally expensive simulations that would be required to directly determine the free energy change associated with PIEZO1's closed→open transition in the presence (ΔG_{gating}^{holo}) and absence (ΔG_{gating}^{apo}) of Yoda1 in the binding site (Fig. 2). A potential limitation of our two-state computational system is the omission of PIEZO1's inactivated state(s). Whether PIEZO1 inactivation modulates Yoda1's binding properties will be an important question to address once structures of inactivated channels become available.

Using three orthogonal computational binding assays, namely, ABFE, RBFE, and SILCS, we show that Yoda1 binds PIEZO1 stronger in the open state, independent of the choice of force fields, simulation engines, and algorithms. The ABFE of Yoda1 computed in the closed state agrees well with the K_d measured experimentally, in line with the expectation that PIEZO1 populates a closed state in the presence of detergent micelles. RBFE data for Yoda1 analogs further provide an underlying thermodynamic rationale for their loss or gain of agonist activity relative to Yoda1. The RBFE protocol and the SAR insights should be valuable for guiding medicinal chemistry design and prioritizing synthesis efforts.

It is worth stressing that large protein conformational changes are not sampled in the short timescale of ABFE simulations. This conveniently allowed us to use a truncated protein model to compute the binding affinity in the open and closed state separately. Interestingly, in both unbiased simulation and ABFE simulations, we found more lipid atoms occupying the open state pocket than the closed state pocket. This differential local binding environment between two states may explain why conventional docking scoring

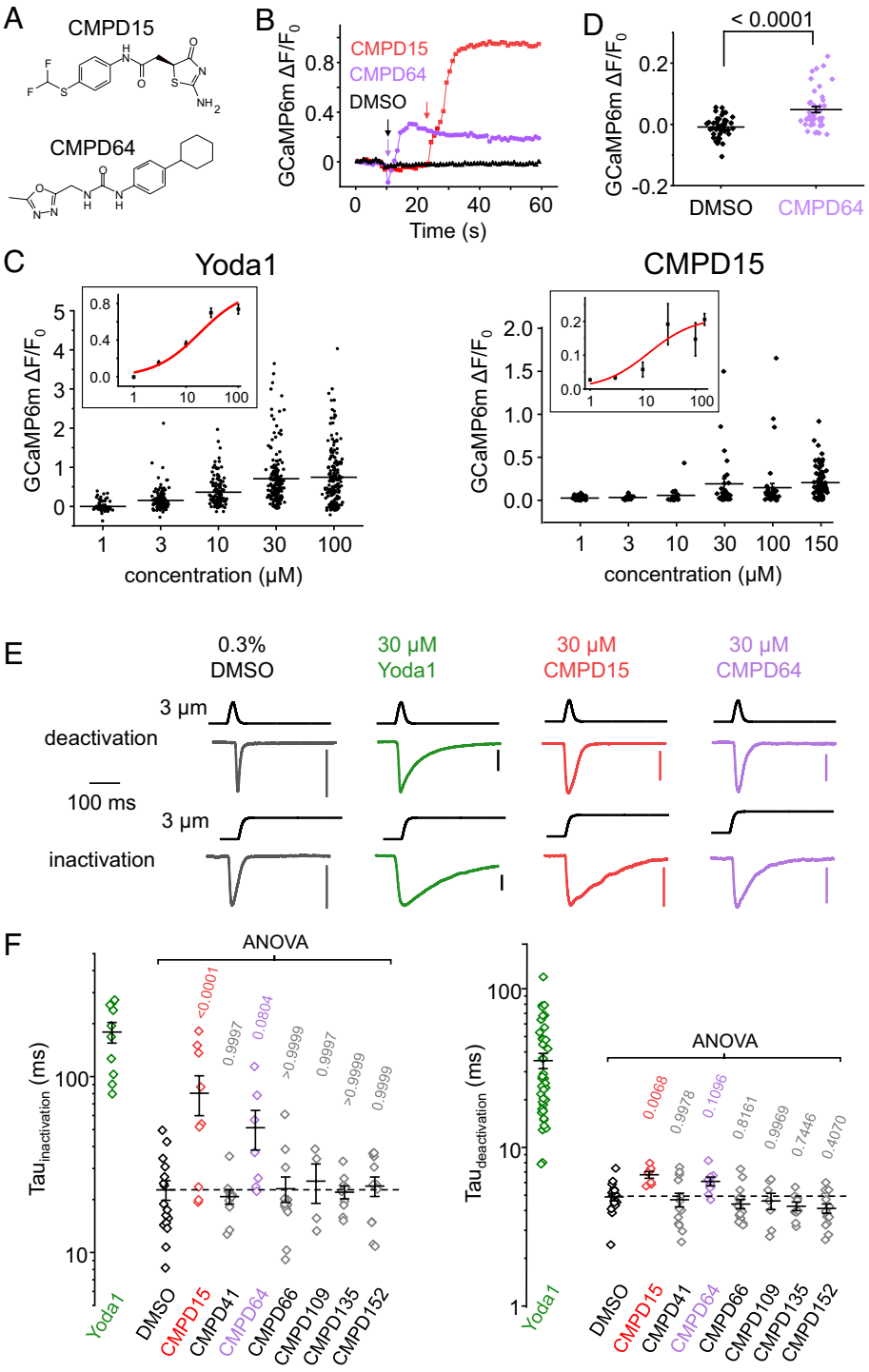

Fig. 5. Identification of PIEZO1 activators. (*A*) Chemical structures of compounds 15 and 64. (*B*) Time course of calcium fluorescence from individual cells acutely exposed to 150 μM of indicated compound or to 0.5% DMSO vehicle control (colored arrows). (*C*) Scatter plots dose–response of calcium uptake for Yoda1 and CMPD15. Dots represent individual cells from 6 (Yoda1) and 3 (CMPD15) independent wells for each tested concentration. Red lines in inserts are fit to the mean using a standard binding function (see *Materials and Methods*, error bars = SEM). (*D*) Scatter plots showing maximal calcium responses from cells acutely treated with 0.5% DMSO or 150 μM CMPD64. Dots represent individual cells from four independent wells. (*E*) Representative whole-cell mPIEZO1 current traces evoked using short (40 ms) or long (500 ms) indentations in the presence of 0.1% DMSO (vehicle control) or 30 μM Yoda1, CMPD15, or CMPD64 (V = −80 mV, vertical bars = 600 pA). (*F*) Scatter plots showing $Tau_{inactivation}$ and $Tau_{deactivation}$ values measured in independent cells in the presence of indicated compounds (30 μM) or DMSO (0.1%) vehicle control. Error bars = SEM. Numbers above plots are exact *P* values from ANOVA with Dunnett's multiple comparison tests. Tau values from cells treated with Yoda1 were excluded from statistical analysis.

functions benchmarked on soluble proteins have led to poor predictions when tested on ion channels (46). Given that SILCS FragMaps are generated in a realistic membrane environment, it represents a promising tool for screening compounds at protein–membrane interfaces.

Our pilot virtual screening using SILCS pharmacophore model of PIEZO1 open state led to the identification of two PIEZO1 activators. Electrophysiological assays show that, like Yoda1, both compounds elicit calcium signals and slow down deactivation/inactivation kinetics. This finding represents a successful identification of PIEZO1

activators based on structure-guided virtual screening. While the hit rate of 1.3% (2 out of 155 candidates showing pharmacological effects) may be considered low, it marks a significant advancement given that Yoda1 was identified from cell-based screening of 3.25 million compounds.

Technically, this low hit rate could be due to the fact that most compounds are silent binders (i.e., binding both open and closed state equally well), a likely possibility since we only selected small molecules based on their ability to virtually bind the open state. In addition, SILCS uses a scoring function that sums up the grid energy of each atom based on their FragMaps location. This kind of additive scoring function is not equivalent to binding free energy and thus can be further optimized. As more compound data become available, SILCS has the potential to combine with Bayesian machine learning algorithms to improve accuracy (46). With improved accuracy, dual virtual screening against both PIEZO1 open and closed states could accelerate the discovery of PIEZO1 agonists and inhibitors in the near future.

Major drug design efforts in the past several decades have been focused on ligands that bind at the protein–aqueous phase, whereas much less attention has been given to ligands that bind at the protein–membrane interface (54). In particular, hydrophobic small molecules targeting ion channels often partition into the membrane to access allosteric binding sites located between transmembrane helices. While the current work does not exclude the possibility of other functionally important binding sites in PIEOZ1, we show that our computational approach has the potential to tackle this drug discovery challenge on multiple levels, from binding site identification, mechanism of action, virtual screening, to lead optimization.

Materials and Methods

Cell Culture and Transfection. PIEZO1-deficient HEK293T$^{\Delta PZ1}$ cells, a gift from Dr. Ardèm Patapoutian (Scripps Research), were cultured at 37 °C and 5% CO2 in Dulbecco's Modified Eagle Medium (GIBCO) supplemented with penicillin–streptomycin and 10% fetal calf serum (Life Technologies). For electrophysiology, HEK293T$^{\Delta PZ}$ cells were seeded into 35-mm cell culture dishes and transiently transfected with a pCDNA3.1-mPIEZO1-IRES-mCherry or with a pCDNA3.1-mPIEZO1 plasmid with Lipofectamine 3000 Transfection Reagent (Life Technologies) using the manufacturer's recommended instructions. For calcium imaging, HEK293T$^{\Delta PZ}$ cells were seeded in 96-well plates and cotransfected at 30 to 50% confluence with 100 ng of a pCDNA3.1-IRES-GcAMP6m plasmid.

Small Molecules. Yoda1 was purchased from Sigma-Aldrich (SML1558), dissolved in DMSO at 40 mM, and stored at −20 °C. Top 155 compounds from the virtual screen were purchased from ChemBridge's Hit2Lead, dissolved in DMSO at a concentration ranging from 10 to 40 mM, and stored at −20 °C. Compounds 15 and 64 were both dissolved at 30 mM in DMSO.

Cloning. Cysteine substitutions were introduced into the mouse PIEZO1 cDNA of the pCDNA3.1-mPIEZO1 plasmid using either the NEBuilder HiFi DNA Assembly Kit (New England Biolabs) or the QuickChange Lightning Multi Site-Directed Mutagenesis Kit (Agilent Technologies). The presence of cysteine mutations was verified by automated Sanger sequencing (Genewiz, Azenta).

Macroscopic Patch-Clamp Recordings. Cells were used 48 to 72 h after transfection. Recording pipettes were pulled to a resistance of 2 to 3 MΩ and fire polished using a microforge (MF2, Narishige). Blunt poking probes were made by fire-polishing the tip of glass pipettes to a size of ~2 to 4 μm. Indentation stimuli were delivered by displacing poking probes at a ~70° angle with a piezoelectric actuator (P-841, Physik Instrumente) controlled by Clampex via an amplifier (E-625, Physik Instrumente). Before experiments, the glass probe was moved until visible contact with the cell. The probe was then retracted approximately 1 to 2 μm to set the initial probe position. Consecutive poking stimuli were delivered using 20-s time intervals to allow recovery from inactivation.

Calcium Imaging. Three to four days after transfection, cells were washed with 100 μL Hank's Balanced Saline Solution (HBSS) and returned to the incubator for 20 min before experiments. GcAMP6m fluorescence was measured using a 100 W mercury lamp, a standard green fluorescence cube, and a 20× objective mounted onto an inverted Eclipse microscope (Nikon). Fluorescence images were acquired at 1 Hz using a DigitalSight camera and the Nikon Digital Element D software. One hundred microliters of a 2× HBSS solution containing 2× concentration of compound of interest or 2× DMSO vehicle control (<1% in all cases) was added to the cells approximately 10 s after the start of the recording. For dose–response plots, data were fitted to a standard binding function:

$$\frac{\Delta F}{F_0} = \frac{E_{max} \times C}{EC_{50} + C} \quad [1]$$

where C is the ligand concentration, Emax is the asymptotic, maximal value of fluorescence the signal, and EC50 is the concentration producing 50% of Emax.

Computational Methods Summary. Three MD-based computational methods were used to compare the binding affinities of Yoda1 and its analogs in PIEZO1 open and closed states. Table 3 provides a summary of key parameters of each method. All codes used in this study are available at https://github.com/LynaLuo-Lab/Piezo1-Ligands-FreeEnergy.

MD Simulation System Preparations. Yoda1 binding pose in closed PIEZO1 conformation was taken from the last frame of previous 4.8 μs MD trajectory (29). The initial binding pose of Yoda1 in PIEZO1 open conformation was generated by aligning the four TM helices (TM29–30 on repeat B, and TM35–36 on repeat A, residue 1683 to 1733 and 2047 to 2097) consisting of the binding site. The PIEZO1 open state was taken the last frame of 2 μs trajectory (7). Dooku1 binding pose is generated by modifying Yoda1 structure in the binding site using MOE software (55). Since the binding affinity is influenced by local protein conformation and local membrane/solvent environment, a single PIEZO1 arm (residue 1131 to 2190, consist of repeat A-C, beam and anchor regions) embedded in the lipid bilayer is used instead of the whole PIEZO1 trimer (Fig. 1). To keep the monomer stable, weak backbone RMSD restraints were applied on the first and last transmembrane helices remote from Yoda1 binding site (*SI Appendix*, Fig. S11). Each protein–ligand complex was prepared in solvated POPC bilayer using CHARMM-GUI (56, 57). CHARMM36 parameter sets were used for the protein (36), ions (58), lipids (59), and TIP3P for water (60). CHARMM general force field (CGenFF) (37, 38) was used for small molecules. The terminal amino acids of PIEZO1 segments are capped using acetylated N-terminal (ACE) and methyl-amidated C-terminal (CT3) blocking groups. The standard MD equilibrium and production simulation protocols are detailed in Supporting Materials. Five independent replicas of 100 ns unbiased MD were first conducted using AMBER20 pmemd.cuda on RTX2080Ti GPU cards for each ligand-protein complex.

Absolute binding free energy (ABFE) Simulations. In the alchemical approach, geometric restraints between protein and ligands are necessary to prevent ligands from wandering away from its binding site as λ approaches zero. To account the flexibility of the Yoda1 and Dooku1 in bound state, we were inspired by a previous work of cholesterol binding (61), in which a set of flat-bottom harmonic restraints were used to ensure unbiased sampling of the fully coupled state during alchemical simulations. We computed the contribution of each restraint to ABFE by expressing the dissociation constant as the ratio of configurational integrals, similar to the work of Deng and Roux (62) (see equation S1 in *SI Appendix*, *Methods*). A comparison among ligand binding poses sampled from unbiased MD, fully coupled state ($\lambda = 1$) and uncoupled state ($\lambda = 0$) with restraints are shown in *SI Appendix*, Fig. S1. The free energy components from the flat-bottom harmonic restraints (*SI Appendix*, Table S1) and the long-range correction (LRC) due to the commonly used 12 Å cutoff distance for computing Lennard-Jones (LJ) potential (*SI Appendix*, Table S2 and Fig. S2), as well as the sampling quality and convergence of the ABFE, are documented in *SI Appendix*, Figs. S3–S9.

Flat-bottom harmonic restraint setup. Two ensemble distributions were computed from a total of 500 ns unbiased trajectories: 1) the distance R between center of mass (COM) of ligand and the binding site and 2) ligand conformational RMSD after rigid-body alignment of the binding site to the initial snapshot, i.e., distance-to-bound-configuration (DBC) in NAMD colvars (61). The boundaries of the flat-bottom harmonic restraint for ligand conformation U_c and protein–ligand distance U_d (force constant 100 kcal/mol/Å^2) are set to be beyond the limit of the

Table 3. Summary of three computational methods

	Absolute binding free energy (ABFE)	Relative binding free energy (RBFE)	SILCS
MD engine	NAMD2.14	AMBER20	GROMACS 2016.4
Methods	FEP/REMD Double decoupling Soft-core potential	AMBET-TI Dual ligand topology Soft-core potential Unified protocol	GCMC/MD
Force field	Charmm36ff, TIP3P, CGenFF	ff19SB, Lipid 17, GAFF2.1, TIP3P	Charmm36ff, TIP3P, CGenFF
Nonbonded parameters	Cutoff 12 Å, PME Long-range correction at 25 Å	Cutoff 10 Å, PME	Cutoff 8 Å, PME
Ensemble	Semi-isotropic NPT (310 K, 1 atm, Langevin thermostat, Langevin piston barostat)	NPT (310 K, 1 atm, Langevin thermostat, Monte Carlo barostat)	Semi-isotropic NPT (300 K, 1 atm, Nose–Hoover thermostat, Parrinello–Rahman barostat); μVT for GCMC
Timestep	2 fs	HMR 4 fs	1 fs
Sampling	6 ns × 128λ Exchange frequency 0.2/ps	4 rep × 5 to 10 ns × 12λ	10 rep × 100 ns
Convergence criteria	Exchange acceptance ratio > 70% Uncorrelated sampling ~1,000 Round-trip time 1 to 2 ns	Forward and reversed free energies agree within error	FragMap overlap coefficients > 0.7 Lowest LGFE scores from 5 independent SILCS-MC docking within 0.5 kcal/mol

ensemble distribution of R and RMSD so that when the ligand is fully coupled ($\lambda = 1$), the free energy contribution of the R and RMSD restraints are negligible.

FEP/REMD setup. ABFEs were calculated with double-decoupling method (34) using FEP/REMD implemented in NAMD2.14 (35). MD-based prediction of binding affinity at TM region requires accurate sampling of the ensemble distributions of ligand, water, protein, and lipids in bound and unbound states. To achieve this goal, we take advantage of the massive paralleled FEP/REMD (35) to sample 128 intermediates between initial (unbound) and final (bound) end states. The soft-core potential was used to scale van der Waals interaction to prevent the occurrence of singularities at small λ values (63). All simulations were conducted at 300 K and 1 bar NPT ensemble. PME is used for long-range electrostatics and short-range cutoff is 12 Å with a smooth switching off between 10 and 12 Å. LRC cutoff is 25 Å (see below).

LRCs. To account for the long-range vdW interaction in nonisotropic binding environment beyond the CHARMM force field standard cutoff distance (12 Å with a smooth switching off between 10 and 12 Å), we recomputed the vdW potential energies using a larger vdW cutoff (25 Å with a smooth switching off between 23 and 25 Å) for every frame sampled in the fully coupled and fully decoupled states in bulk and in binding site. Specifically, we used the exponential averaging approach (also known as the Zwanzig relation) (64), in which $\Delta G^{LRC} = \Delta E_{\lambda=1} - \Delta E_{\lambda=0} = -k_B T \ln \langle e^{-(E^{LR}_{\lambda=1} - E^{SR}_{\lambda=1})/k_B T} \rangle + k_B T \ln \langle e^{-(E^{LR}_{\lambda=0} - E^{SR}_{\lambda=0})/k_B T} \rangle$. The average vdW energy $\langle E \rangle$ computed at different LJ cutoff distances from FEP/REMD simulations are plotted in *SI Appendix*, Fig. S2 and listed in *SI Appendix*, Table S2. The ABFE results with and without LRCs are listed in *SI Appendix*, Table S1. The LRCs contributed equally to ΔG^{bulk}_{int} and ΔG^{site}_{int} in closed state, thus do not change the binding affinity of Yoda1 and Dooku1 in the closed state. LRC's contribution to ΔG^{site}_{int} in open state is larger (−2.6 kcal/mol in Yoda1 and −2.1 kcal/mol in Dooku1), thus makes the binding affinity of Yoda1 and Dooku1 in the open state about 1 kcal/mol more favorable than the ABFE without LRC. Overall, the ABFE results with and without LRCs reach the same conclusion that Yoda1 binds to the open state stronger than the closed state, and Dooku1 binds to the closed state stronger than the open state.

Convergence of ABFE. Yoda1 or Dooku1 is gradually decoupled from the binding site (128 λ intermediates) and bulk solvent (64 λ intermediates). The time evolution of the FEP/REMD results suggests that a plateau is reached within 4 to 6 ns/replica for all six protein–ligand systems (*SI Appendix*, Fig. S3). We considered that the FEP/REMD simulation approximates convergence when that last two 0.5 ns running average of free energy value fluctuates within 0.5 kcal/mol. Neighboring replica exchange was attempted at every 100 steps (0.2 ps) and yielded >70% acceptance ratios for all systems (*SI Appendix*, Fig. S4). The numbers of uncorrelated sampling per replica are plotted in *SI Appendix*, Fig. S5. Round trip time is about 2 ns (*SI Appendix*, Figs. S6 and S7). The convergence of RMSD restraint free energy at $\lambda = 0$ is plotted in *SI Appendix*, Fig. S8. The final results and uncertainties are summarized in *SI Appendix*, Table S1.

Relative binding free energy (RBFE) Simulations. RBFEs were calculated using the same systems as in ABFE calculations, including membrane and water. The coordinates of the PIEZO1 open and closed systems were taken from ABFE simulations and used as starting points for RBFE calculations with thermodynamic integration (TI) (65) method in AMBER. The AMBER force field [ff19SB (43) for protein, GAFF2.1 (44) for ligand, and Lipid17 for lipids] was used for all the simulation systems. Antechamber and parmchk2 were used to parameterize the ligands and their charges were calculated using AM1-BCC (66) for GAFF2.1. LEaP was used to generate topology file (.parm7) and coordinate file (.rst7). In the end, Parmed (67) was used to apply hydrogen mass repartitioning (HMR) to the system.

Each transformation pair system was generated with unified protocol in which both electrostatic and vdW interactions are scaled simultaneously by the softcore potentials (41, 42). The RBFE between two ligands (L0 to L1) is calculated as

$$\Delta\Delta G^{L0\to L1}_{bind} = \Delta G^{L0\to L1}_{complex} - \Delta G^{L0\to L1}_{ligand}, \quad [2]$$

where $\Delta G^{L0\to L1}_{complex}$ and $\Delta G^{L0\to L1}_{ligand}$ are the alchemical transformations of L0 to L1 in the complex and solution, respectively. The free energy difference between states L0 and L1 can be estimated as

$$\Delta G^{L0\to L1}_{complex/ligand} = \int_0^1 \left\langle \frac{\partial U(\lambda)}{\partial \lambda} \right\rangle d\lambda, \quad [3]$$

where $U(\lambda)$ is the λ-coupled potential energy and λ is a coupling parameter varying from 0 to 1. The integration is calculated via the average of the λ derivative of the coupled potential energy at each intermediate λ state. The ΔG values are obtained by the sum of numerical integration over the number of λ windows quadrature points with associated weights of $\partial U/\partial\lambda$. Long-range electrostatics was treated with the particle mesh Ewald (PME) method, and the van der Waals interactions were calculated with a cutoff distance of 10 Å (68, 69). The second-order smoothstep softcore potential was applied in the simulation (41). The values of 0.2 and 50 Å^2 were used for the parameters α and β of the softcore potential. Equilibration was performed for 5 ps employing the NPT ensemble after minimization in each λ window. AMBER-TI simulations were performed in the NPT ensemble at 310 K and 1 atm with the pmemd.cuda module of AMBER20 (41). Pressure was regulated by isotropic MC barostat with a pressure relaxation time of 2.0 ps. All alchemical transformations were done using the unified protocol with a 4-fs time step with HMR (70).

Convergence of RBFE. Twelve windows (0.0000, 0.0479, 0.1151, 0.2063, 0.3161, 0.4374, 0.5626, 0.6839, 0.7937, 0.8850, 0.9521, and 1.0000) were employed for each complex and solution system. Five nanosecond AMBER-TI simulations were performed for each λ window and the last 4 ns was used to calculate the final $\Delta\Delta G_{bind}$. For the transformation pair from Yoda1 to Dooku1 in the closed state, 10 ns AMBER-TI simulations were performed for each λ window to ensure the estimated $\Delta\Delta G_{bind}$ value is obtained from the converged trajectories. For this transformation pair, the last 5 ns of AMBER-TI simulations were used to estimate the $\Delta\Delta G_{bind}$. Four independent runs for each $\Delta\Delta G_{bind}$ were performed for statistical analysis. Convergence plots for each transformation are provided in *SI Appendix*, Fig. S10. For convergence analysis, the trajectories used for the final $\Delta\Delta G_{bind}$ were divided into 12 blocks to estimate the cumulative average $\Delta\Delta G_{bind}$ in the forward direction. The cumulative $\Delta\Delta G_{bind}$ values were obtained from the time-reversed data starting from the end of trajectories but using the same amount of simulation time (71). The forward and time-reversed free energy estimations agree within error, indicating that our AMBER-TI simulations are converged well (72).

Site Identification by Ligand Competitive Saturation. SILCS simulations were performed using GROMACS 2016.4 simulation program (73), in which Grand Canonical Monte Carlo (GCMC) samples water and small drug fragments, with the subsequent MD simulation for the sampling of protein conformational dynamics (47). The drug fragments used in this study include benzene, propane, methanol, formamide, imidazole, acetaldehyde, methylammonium, and acetate in standard version and fluoroethane, trifluoroethane, chloroethane, fluorobenzene, chlorobenzene, and bromobenzene in halogen version. During the simulations, these functional groups and water molecules compete to bind the protein and membrane. From 10 replicas of 100 ns trajectories, the three-dimensional (3D) probability distributions of each fragment, called FragMaps, were calculated and then converted into Grid Free Energy (GFE) based on a Boltzmann inversion. Force field for protein, water, ions, and small molecules remains the same as in FEP calculations. The overlap coefficients are between 0.75 to 0.97 for all FragMaps obtained in current study.

The Monte Carlo–based SILCS (SILCS-MC) docking protocol (31) was applied to predict ligand binding poses based FragMaps. In this study, we utilized a full version of FragMaps with standard maps for generic apolar (benzene, propane C), generic H-bond donor [methanol O, formamide N, imidazole (NH)] and acceptor (methanol O, formamide O, imidazole N, acetaldehyde O), negatively charged (acetate) and positively charged (methylammonium) and halogen maps for fluoroethane fluorine (FETX), trifluoroethane carbon (TFEC), fluorobenzene fluorine (FLBX), chloroethane chlorine (CLEX), chlorobenzene chlorine (CLBX), bromobenzene bromine (BRBX), and dimethyl ether oxygen (DMEO) to supplement the 2018 generic halogen atom classification scheme (ACS) for scoring. With the improved treatment of halogens in CGenFF, halogen maps are used to reproduce the σ-holes and improve halogen bonding.

For each docking, five independent SILCS-MC runs were performed with a two-step mode. Each SILCS-MC run involved a long-local MC protocol of 250 cycles of 10,000 Metropolis MC steps and 40,000 steps of simulated annealing (SA) from initial aligned structures. MC steps sample a wide range of binding poses with step size of 1 Å for translations, 180° for maximal rigid rotations per step and 180° for maximal dihedral angle rotations per step. This setup is to ensure sufficient sampling of ligand poses at the binding pocket. SA steps are designed to find a local minimum with the acceptance criteria defined by the Ligand Grid Free Energies (LGFE). SA involved maximum ranges of step size of 0.2 Å for translations, 9° for maximal rigid rotations per step and 9° for maximal dihedral angle rotations per step with gradual cooling from 300 to 0 K. The SILCS-MC runs were repeated for five times during which each cycle initiated with a different random seed and was repeated until it finished 250 cycles or reached convergence. The lowest LGFE and average LGFE scores from the minimum score in five independent jobs were obtained.

SILCS Virtual Screening. We used the SILCS-PHARM software (SilcsBio, LLC) (49) to convert the SILCS FragMaps at Yoda1 binding region into pharmacophore features using a clustering algorithm in combination with energetic criteria. A subset of pharmacophore features is used to search the compound library of ~8 million commercially available compounds (provided by MolPort), using the program Pharmer (50) based on matches between the pharmacophore input features and ligand functional groups. To enable an efficient search, it is necessary to pregenerate multiple conformations of each ligand in the library. The conformational library was generated to create a minimum of 10 distinct conformers of each ligand. The program Pharmer then aligns the functional groups for each conformation with the input pharmacophore and returns the conformation with the lowest rmsd. To refine the returned conformers, we employed SILCS-MC (31) and performed a short pose refinement starting from the input conformation. The conformers were subsequently scored based on the LGFE scores using the FragMaps. Instead of selecting top-scoring compounds, we used three different selection criteria to increase the diversity of hit compounds. For the first selection, the compounds having LGFE score > -10 kcal/mol were removed and the remaining compounds were clustered using extended-connectivity fingerprints (ECFPs) (74) of radius 2 and Tanimoto index cutoff of 0.6. Fifty five representative compounds from each cluster were purchased. For the second selection, 50 compounds dissimilar from the first selection (Tanimoto index < 0.6) and having high solubility (Log Solubility > -4) were purchased. For the last selection, 50 compounds dissimilar from the first and the second set of compounds (Tanimoto index < 0.6) and medium solubility (Log Solubility > -6) and rigidity (number of rotatable bonds < 5) were purchased.

Data, Materials, and Software Availability. The NAMD and AMBER topology files, input and output files for ABFE and RBFE simulations and data analysis, SILCS FragMaps of PIEZO1 open state, together with docking poses and pharmacophore are available to at https://github.com/LynaLuo-Lab/Piezo1-Ligands-FreeEnergy (DOI: 10.5281/zenodo.8329438) (75).

ACKNOWLEDGMENTS. This work was supported by NIH grants GM130834 (Y.L.L. and J.J.L.) and GM138472 (W.I.). Computational resources for ABFE calculations were provided by NSF XSEDE research allocation MCB160119 (Y.L.L.). We would like to thank the SilcsBio team, especially Dr. Alexander MacKerell for his critical insights and suggestions.

Author affiliations: [a]Department of Biotechnology and Pharmaceutical Sciences, Western University of Health Sciences, Pomona, CA 91766; [b]Department of Basic Medical Sciences, Western University of Health Sciences, Pomona, CA 91766; [c]Department of Biological Sciences, Lehigh University, Bethlehem, PA 18015; [d]Department of Chemistry, Lehigh University, Bethlehem, PA 18015; [e]Department of Bioengineering, Lehigh University, Bethlehem, PA 18015; [f]Department of Computer Science and Engineering, Lehigh University, Bethlehem, PA 18015; and [g]Department of Pharmaceutical Sciences, University of Maryland, Baltimore, MD 21201

1. J. M. Kefauver, A. B. Ward, A. Patapoutian, Discoveries in structure and physiology of mechanically activated ion channels. *Nature* **587**, 567–576 (2020).
2. L. Wang *et al.*, Structure and mechanogating of the mammalian tactile channel PIEZO2. *Nature* **573**, 225–229 (2019).
3. K. Saotome *et al.*, Structure of the mechanically activated ion channel Piezo1. *Nature* **554**, 481–486 (2018).
4. Q. Zhao *et al.*, Structure and mechanogating mechanism of the Piezo1 channel. *Nature* **554**, 487–492 (2018).
5. Y. R. Guo, R. MacKinnon, Structure-based membrane dome mechanism for Piezo mechanosensitivity. *Elife* **6**, e33660 (2017).
6. X. Yang *et al.*, Structure deformation and curvature sensing of PIEZO1 in lipid membranes. *Nature* **604**, 377–383 (2022), 10.1038/s41586-022-04574-8.
7. W. Jiang *et al.*, Crowding-induced opening of the mechanosensitive Piezo1 channel in silico. *Commun. Biol.* **4**, 84 (2021).
8. Y. C. Lin *et al.*, Force-induced conformational changes in PIEZO1. *Nature* **573**, 230–234 (2019).
9. Y. Wang *et al.*, A lever-like transduction pathway for long-distance chemical- and mechano-gating of the mechanosensitive Piezo1 channel. *Nat. Commun.* **9**, 1300 (2018).
10. D. De Vecchis, D. J. Beech, A. C. Kalli, Molecular dynamics simulations of Piezo1 channel opening by increases in membrane tension. *Biophys. J.* **120**, 1510–1521 (2021).
11. C. D. Cox *et al.*, Removal of the mechanoprotective influence of the cytoskeleton reveals PIEZO1 is gated by bilayer tension. *Nat. Commun.* **7**, 10366 (2016).
12. A. H. Lewis, J. Grandl, Mechanical sensitivity of Piezo1 ion channels can be tuned by cellular membrane tension. *Elife* **4**, e12088 (2015).
13. D. J. Beech, Endothelial Piezo1 channels as sensors of exercise. *J. Physiol.* **596**, 979–984 (2018).
14. C. N. Nguetse *et al.*, A common polymorphism in the mechanosensitive ion channel PIEZO1 is associated with protection from severe malaria in humans. *Proc. Natl. Acad. Sci. U.S.A.* **117**, 9074–9081 (2020).
15. S. Ma *et al.*, Common PIEZO1 allele in African populations causes RBC dehydration and attenuates plasmodium infection. *Cell* **173**, 443–455.e412 (2018).
16. D. Choi *et al.*, Piezo1 incorporates mechanical force signals into the genetic program that governs lymphatic valve development and maintenance. *JCI Insight* **4**, e125068 (2019).
17. K. Nonomura *et al.*, Mechanically activated ion channel PIEZO1 is required for lymphatic valve formation. *Proc. Natl. Acad. Sci. U.S.A.* **115**, 12817–12822 (2018), 10.1073/pnas.1817070115.

18. A. Bosutti *et al.*, "Time window" effect of Yoda1-evoked Piezo1 channel activity during mouse skeletal muscle differentiation. *Acta Physiol. (Oxf)* **233**, e13702 (2021), 10.1111/apha.13702.
19. W. J. Sun *et al.*, The mechanosensitive Piezo1 channel is required for bone formation. *Elife* **8**, e47454 (2019).
20. W. Lee *et al.*, Synergy between Piezo1 and Piezo2 channels confers high-strain mechanosensitivity to articular cartilage. *Proc. Natl. Acad. Sci. U.S.A.* **111**, E5114–5122 (2014).
21. J. M. Romac, R. A. Shahid, S. M. Swain, S. R. Vigna, R. A. Liddle, Piezo1 is a mechanically activated ion channel and mediates pressure induced pancreatitis. *Nat. Commun.* **9**, 1715 (2018).
22. R. Z. Hill, M. C. Loud, A. E. Dubin, B. Peet, A. Patapoutian, PIEZO1 transduces mechanical itch in mice. *Nature* **607**, 104–110 (2022), 10.1038/s41586-022-04860-5.
23. M. Luo *et al.*, Compression enhances invasive phenotype and matrix degradation of breast Cancer cells via Piezo1 activation. *BMC Mol. Cell Biol.* **23**, 1 (2022).
24. J. Zhang *et al.*, PIEZO1 functions as a potential oncogene by promoting cell proliferation and migration in gastric carcinogenesis. *Mol. Carcinog.* **57**, 1144–1155 (2018), 10.1002/mc.22831.
25. C. Li *et al.*, Piezo1 forms mechanosensitive ion channels in the human MCF-7 breast cancer cell line. *Sci. Rep.* **5**, 8364 (2015).
26. R. Syeda *et al.*, Chemical activation of the mechanotransduction channel Piezo1. *Elife* **4**, e07369 (2015).
27. T. D. Wijerathne, A. D. Ozkan, J. J. Lacroix, Yoda1's energetic footprint on Piezo1 channels and its modulation by voltage and temperature. *Proc. Natl. Acad. Sci. U.S.A.* **119**, e2202269119 (2022).
28. J. J. Lacroix, W. M. Botello-Smith, Y. Luo, Probing the gating mechanism of the mechanosensitive channel Piezo1 with the small molecule Yoda1. *Nat. Commun.* **9**, 2029 (2018).
29. W. M. Botello-Smith *et al.*, A mechanism for the activation of the mechanosensitive Piezo1 channel by the small molecule Yoda1. *Nat. Commun.* **10**, 4503 (2019).
30. O. Guvench, A. D. MacKerell Jr., Computational fragment-based binding site identification by ligand competitive saturation. *PLoS Comput. Biol.* **5**, e1000435 (2009).
31. C. E. Faller, E. P. Raman, A. D. MacKerell Jr., O. Guvench, Site Identification by Ligand Competitive Saturation (SILCS) simulations for fragment-based drug design. *Methods Mol. Biol.* **1289**, 75–87 (2015).
32. J. Jumper *et al.*, Highly accurate protein structure prediction with AlphaFold. *Nature* **596**, 583–589 (2021).
33. V. Lukacs *et al.*, Impaired PIEZO1 function in patients with a novel autosomal recessive congenital lymphatic dysplasia. *Nat. Commun.* **6**, 8329 (2015).
34. M. K. Gilson, J. A. Given, B. L. Bush, J. A. McCammon, The statistical-thermodynamic basis for computation of binding affinities: A critical review. *Biophys. J.* **72**, 1047–1069 (1997).
35. W. Jiang, M. Hodoscek, B. Roux, Computation of absolute hydration and binding free energy with free energy perturbation distributed replica-exchange molecular dynamics. *J. Chem. Theory Comput.* **5**, 2583–2588 (2009).
36. A. D. Mackerell Jr., M. Feig, C. L. Brooks III, Extending the treatment of backbone energetics in protein force fields: Limitations of gas-phase quantum mechanics in reproducing protein conformational distributions in molecular dynamics simulations. *J. Comput. Chem.* **25**, 1400–1415 (2004).
37. K. Vanommeslaeghe *et al.*, CHARMM general force field: A force field for drug-like molecules compatible with the CHARMM all-atom additive biological force fields. *J. Comput. Chem.* **31**, 671–690 (2010).
38. W. Yu, X. He, K. Vanommeslaeghe, A. D. MacKerell Jr., Extension of the CHARMM general force field to sulfonyl-containing compounds and its utility in biomolecular simulations. *J. Comput. Chem.* **33**, 2451–2468 (2012).
39. E. L. Evans *et al.*, Yoda1 analogue (Dooku1) which antagonizes Yoda1-evoked activation of Piezo1 and aortic relaxation. *Br J. Pharmacol.* **175**, 1744–1759 (2018).
40. H. Tang *et al.*, Piezo-type mechanosensitive ion channel component 1 (Piezo1): A promising therapeutic target and its modulators. *J. Med. Chem.* **65**, 6441–6453 (2022).
41. T. S. Lee *et al.*, Alchemical binding free energy calculations in AMBER20: Advances and best practices for drug discovery. *J. Chem. Inf Model* **60**, 5595–5623 (2020).
42. H. Zhang *et al.*, CHARMM-GUI free energy calculator for practical ligand binding free energy simulations with AMBER. *J. Chem. Inf. Model* **61**, 4145–4151 (2021).
43. C. Tian *et al.*, ff19SB: Amino-acid-specific protein backbone parameters trained against quantum mechanics energy surfaces in solution. *J. Chem. Theory Comput.* **16**, 528–552 (2020).
44. X. He, V. H. Man, W. Yang, T. S. Lee, J. Wang, A fast and high-quality charge model for the next generation general AMBER force field. *J. Chem. Phys.* **153**, 114502 (2020).
45. Y. Yang *et al.*, Efficient exploration of chemical space with docking and deep learning. *J. Chem. Theory Comput.* **17**, 7106–7119 (2021).
46. M. Mousaei, M. Kudaibergenova, A. D. MacKerell Jr., S. Noskov, Assessing hERG1 blockade from Bayesian machine-learning-optimized site identification by ligand competitive saturation simulations. *J. Chem. Inf Model* **60**, 6489–6501 (2020).
47. S. K. Lakkaraju, E. P. Raman, W. Yu, A. D. MacKerell Jr., Sampling of organic solutes in aqueous and heterogeneous environments using oscillating excess chemical potentials in grand canonical-like monte carlo-molecular dynamics simulations. *J. Chem. Theory Comput.* **10**, 2281–2290 (2014).
48. O. Trott, A. J. Olson, AutoDock Vina: Improving the speed and accuracy of docking with a new scoring function, efficient optimization, and multithreading. *J. Comput. Chem.* **31**, 455–461 (2010).
49. W. Yu, S. K. Lakkaraju, E. P. Raman, L. Fang, A. D. MacKerell Jr., Pharmacophore modeling using site-identification by ligand competitive saturation (SILCS) with multiple probe molecules. *J. Chem. Inf. Model.* **55**, 407–420 (2015).
50. D. R. Koes, C. J. Camacho, Pharmer: Efficient and exact pharmacophore search. *J. Chem. Inf Model* **51**, 1307–1314 (2011).
51. G. Parsonage *et al.*, Improved PIEZO1 agonism through 4-benzoic acid modification of Yoda1. *Br. J. Pharmacol.* **180**, 2039–2063 (2022), 10.1111/bph.15996.
52. T. D. Wijerathne, A. D. Ozkan, J. J. Lacroix, Microscopic mechanism of PIEZO1 activation by pressure-induced membrane stretch. *J. Gen. Physiol.* **155**, e202213260 (2023).
53. E. D. Nosyreva, D. Thompson, R. Syeda, Identification and functional characterization of the Piezo1 channel pore domain. *J. Biol. Chem.* **296**, 100225 (2020). 10.1074/jbc.RA120.015905.
54. J. Payandeh, M. Volgraf, Ligand binding at the protein–lipid interface: Strategic considerations for drug design. *Nat. Rev. Drug Discov.* **20**, 710–722 (2021).
55. Molecular Operating Environment (MOE), 2022.02 Chemical Computing Group ULC (Montreal, Canada, 2023).
56. J. Lee *et al.*, CHARMM-GUI input generator for NAMD, GROMACS, AMBER, OpenMM, and CHARMM/OpenMM simulations using the CHARMM36 additive force field. *J. Chem. Theory Comput.* **12**, 405–413 (2016).
57. S. Jo, T. Kim, V. G. Iyer, W. Im, CHARMM-GUI: A web-based graphical user interface for CHARMM. *J. Comput. Chem.* **29**, 1859–1865 (2008).
58. A. D. MacKerell Jr. *et al.*, All-atom empirical potential for molecular modeling and dynamics studies of proteins. *J. Phys. Chem. B* **102**, 3586–3616 (1998).
59. J. B. Klauda *et al.*, Update of the CHARMM all-atom additive force field for lipids: Validation on six lipid types. *J. Phys. Chem. B* **114**, 7830–7843 (2010).
60. W. L. Jorgensen, J. Chandrasekhar, J. D. Madura, R. W. Impey, M. L. Klein, Comparison of simple potential functions for simulating liquid water. *J. Chem. Phys.* **79**, 926–935 (1983).
61. R. Salari, T. Joseph, R. Lohia, J. Hénin, G. Brannigan, A streamlined, general approach for computing ligand binding free energies and its application to GPCR-bound cholesterol. *J. Chem. Theory Comput.* **14**, 6560–6573 (2018).
62. Y. Q. Deng, B. Roux, Calculation of standard binding free energies: Aromatic molecules in the T4 lysozyme L99A mutant. *J. Chem. Theory Comput.* **2**, 1255–1273 (2006).
63. M. Zacharias, T. P. Straatsma, J. A. Mccammon, Separation-shifted scaling, a new scaling method for lennard-jones interactions in thermodynamic integration. *J. Chem. Phys.* **100**, 9025–9031 (1994).
64. M. R. Shirts, D. L. Mobley, J. D. Chodera, V. S. Pande, Accurate and efficient corrections for missing dispersion interactions in molecular simulations. *J. Phys. Chem. B* **111**, 13052–13063 (2007).
65. J. Kumar, T. K. Dey, S. K. Sinha, Semiclassical statistical mechanics of hard-body fluid mixtures. *J. Chem. Phys.* **122**, 224504 (2005).
66. A. Jakalian, D. B. Jack, C. I. Bayly, Fast, efficient generation of high-quality atomic charges. AM1-BCC model: II. Parameterization and validation. *J. Comput. Chem.* **23**, 1623–1641 (2002).
67. M. R. Shirts *et al.*, Lessons learned from comparing molecular dynamics engines on the SAMPL5 dataset. *J. Comput. Aided Mol. Des.* **31**, 147–161 (2017).
68. T. Darden, D. York, L. Pedersen, Particle mesh Ewald—an N. Log(N) method for Ewald sums in large systems. *J. Chem. Phys.* **98**, 10089–10092 (1993).
69. U. Essmann *et al.*, A smooth particle mesh Ewald method. *J. Chem. Phys.* **103**, 8577–8593 (1995).
70. C. W. Hopkins, S. Le Grand, R. C. Walker, A. E. Roitberg, Long-time-step molecular dynamics through hydrogen mass repartitioning. *J. Chem. Theory Comput.* **11**, 1864–1874 (2015).
71. W. Yang, R. Bitetti-Putzer, M. Karplus, Free energy simulations: Use of reverse cumulative averaging to determine the equilibrated region and the time required for convergence. *J. Chem. Phys.* **120**, 2618–2628 (2004).
72. P. V. Klimovich, M. R. Shirts, D. L. Mobley, Guidelines for the analysis of free energy calculations. *J. Comput. Aid Mol. Des.* **29**, 397–411 (2015).
73. B. Hess, C. Kutzner, D. van der Spoel, E. Lindahl, GROMACS 4: Algorithms for highly efficient, load-balanced, and scalable molecular simulation. *J. Chem. Theory Comput.* **4**, 435–447 (2008).
74. D. Rogers, M. Hahn, Extended-connectivity fingerprints. *J. Chem. Inf. Model* **50**, 742–754 (2010).
75. Y. L. Luo, W. Jiang, H. Zhang, LynaLuo-Lab/Piezo1-Ligands-FreeEnergy: Piezo1-Ligands-FreeEnergy. Zenodo. https://zenodo.org/records/8329438. Deposited 8 September 2023.